Tailbeat perturbations improve swimming efficiency by reducing the phase lag between body motion and the resulting fluid response

Li-Ming Chao (ID)[a,b,c], Laibing Jia (ID)[d,*], Siyuan Wang (ID)[a,b,c], Alexander Liberzon (ID)[e], Sridhar Ravi (ID)[f], Iain D. Couzin (ID)[a,b,c] and Liang Li (ID)[a,b,c,*]

[a]Department of Collective Behaviour, Max Planck Institute of Animal Behavior, Konstanz 78464, Germany
[b]Centre for the Advanced Study of Collective Behaviour, University of Konstanz, Konstanz 78464, Germany
[c]Department of Biology, University of Konstanz, Konstanz 78464, Germany
[d]Department of Naval Architecture, Ocean and Marine Engineering, University of Strathclyde, Glasgow G4 0LZ, UK
[e]School of Mechanical Engineering, Tel Aviv University, Tel Aviv 69978, Israel
[f]School of Engineering and Information Technology, University of New South Wales, Canberra, ACT 2610, Australia
*To whom correspondence should be addressed: Email: l.jia@strath.ac.uk (L.J.); Email: lli@ab.mpg.de (L.L.)
Edited By: Gary Grest

Abstract

Understanding how animals swim efficiently and generate high thrust in complex fluid environments is of considerable interest to researchers in various fields, including biology, physics, and engineering. However, the influence of often-overlooked perturbations on swimming fish remains largely unexplored. Here, we investigate the propulsion generated by oscillating tailbeats with superimposed rhythmic perturbations of high frequency and low amplitude. We reveal, using a combination of experiments in a biomimetic fish-like robotic platform, computational fluid dynamics simulations, and theoretical analysis, that rhythmic perturbations can significantly increase both swimming efficiency and thrust production. The introduction of perturbations increases pressure-induced thrust, while reduced phase lag between body motion and the subsequent fluid dynamics response improves swimming efficiency. Moreover, our findings suggest that beneficial perturbations are sensitive to kinematic parameters, resolving previous conflicts regarding the effects of such perturbations. Our results highlight the potential benefits of introducing perturbations in propulsion generators, providing potential hypotheses for living systems and inspiring the design of artificial flapping-based propulsion systems.

Keywords: swimming efficiency, perturbations, hydrodynamics, computational fluid dynamics, robotics

Significance Statement

From birds in the sky to fish beneath the water, organisms exemplify efficient movement through flapping propulsion. Understanding the mechanism behind this high-efficiency propulsion is invaluable across biological studies, fluid mechanics, and engineering. In our study, by superimposing high-frequency, low-amplitude rhythmic perturbations to a basic flapping oscillation, we surprisingly found both thrust and swimming efficiency could be improved in robotic experiments and computational fluid dynamics simulations. Further analyses suggest that superimposing these rhythmic perturbations amplifies the pressure-induced thrust, and reduces phase lag between body motion and fluid dynamics response, thereby boosting swimming efficiency. Our study hypothesizes that biology may employ similar mechanisms to optimize efficiency and provides a mechanism for engineers to design highly efficient vehicles driven by flapping.

Introduction

Fish have evolved exceptional swimming abilities over almost half a billion years of evolution (1, 2), which has drawn significant interest from various fields such as biology, engineering, physics, and mathematics (3–5). Previous research has shown that fish can enhance their swimming efficiency through a variety of adaptations, including reducing drag with refined surface structures (6–8), harnessing energy from flows created by nearby fish (9–14), adjusting the flexibility of their tail (15–18), and optimizing their swimming movements (19–22).

Being so fundamental, how fish optimize swimming kinematics to enhance swimming efficiency has been widely explored over the past decades (23). A prevailing understanding from biological (24–27) and physical (28, 29) investigations has revealed that swimming in a Strouhal number (defined as $St = 2fA/U$, where f is the swimming frequency, A denotes tailbeats amplitude, and U refers to the swimming velocity) of 0.2–0.4 allows individuals to achieve optimal swimming efficiency. Besides Strouhal number, other studies have shown that swimming efficiency also benefits from other kinematic properties, such as the amplitude of

tailbeat (30), the reduced frequency (normalized swimming frequency) (31), and the profile of oscillating waveforms (e.g. nonsinusoidal (32, 33) and quasisymmetric oscillations (34, 35)). Saadat et al. (30) revealed that a Strouhal number of 0.2–0.4 in combination with an amplitude of approximately 20% of the body length can lead to efficient propulsion. Floryan et al. (31) found, within a specific Strouhal number, the smaller the reduced frequency, the higher the propulsion efficiency.

Most current studies on swimming kinematics and performance assume that the swimmer's movements can be described using various idealized sinusoidal oscillations. However, in nature, swimmers do not use such "clean" kinematic oscillations to move forward. With fast Fourier transform algorithm, natural kinematic oscillations can be resolved into basic and high-frequency components. In most studies, the high-frequency components, which are typically low in amplitude, are often disregarded in simplified body wave models due to their similarity to noise (36). As a result, few studies have investigated the role of these high-frequency and low-amplitude perturbations in kinematics (37, 38). Lehn et al. (37) found that combining high-frequency and low-amplitude perturbations to flexible flapping foils can increase thrust and efficiency. However, it is unclear whether this improvement is mainly due to the flexibility of the foil or the perturbations, as certain stiffness of the foil can also significantly improve efficiency (15–17). Furthermore, some studies that examined the performance of a flapping rigid foil found that perturbations can enhance thrust but not the efficiency of swimming (38), thus calling into question the mechanism that allows for increased efficiency with perturbations. In addition, previous studies have primarily investigated how perturbation frequency impacts swimming efficiency, while there is a lack of research exploring the effect of perturbation amplitude, to thrust production and efficiency, as well as the combined impact of both frequency and amplitude. Overall, it is still largely unknown whether a swimmer with perturbations can improve thrust and efficiency simultaneously, and if so, what kind of perturbations are beneficial and how they lead to improvement. In this work, we combined experimental, numerical, and theoretical studies to systematically explore the benefits of perturbations over the swimmer's performance (Fig. S1).

## Results

Robotic fish experiments

To investigate the general function of small kinematic perturbations to tailbeats during fish-like swimming, we consider perturbations with high frequency and low amplitude compared to a basic sinusoidal wave motion performed by the tail (Fig. 1A and B).

Three modes are defined: basic mode (BM) with a sinusoidal wave representing rhythmic tailbeats (Fig. 1A), perturbation mode (PM) that consists of high-frequency and low-amplitude oscillations (Fig. 1A), and accumulated mode (AM), which represents the combination of sinusoidal wave (BM) and perturbations (PM) (Fig. 1B):

$$
\begin{aligned}
\theta_{bm}(t) &= \Theta_{bm} \sin(2\pi f_{bm} t) \quad \text{BM,} \\
\theta_{pm}(t) &= \Theta_{pm} \sin(2\pi f_{pm} t) \quad \text{PM,} \quad (1)\\
\theta_{am}(t) &= \theta_{bm}(t) + \theta_{pm}(t) \quad \text{AM,}
\end{aligned}
$$

where subscripts bm, pm, and am refer to the parameters in basic mode (BM), perturbation mode (PM), and accumulated mode (AM), respectively. Θ_{bm} and Θ_{pm} are the foil's oscillation angle amplitude in the BM and PM, respectively. f_{bm} and f_{pm} refer to the oscillating frequency in the BM and PM, respectively, and t is the instantaneous time. To control the frequency and amplitude of the perturbation, we introduce dimensionless frequency $\tilde{f} = f_{pm}/f_{bm}$ and amplitude $\tilde{A} = A_{pm}/A_{bm} \approx \Theta_{pm}/\Theta_{bm}$ (see Materials and methods for details), respectively. The Strouhal number ratio is $\tilde{St} = St_{pm}/St_{bm}$, where $St_{bm} = 2f_{bm}A_{bm}/U$ and $St_{pm} = 2f_{pm}A_{pm}/U$ represent the BM-based and PM-based Strouhal numbers, respectively.

Experiments were performed with a robotic fish swimming in a flow tank that was tethered to a high-resolution force sensor. The robotic fish consisted of a high-fidelity goldfish-like body that was capable of replicating various tailbeat kinematics (see Materials and methods; Fig. 1C). We established the basic tailbeat mode
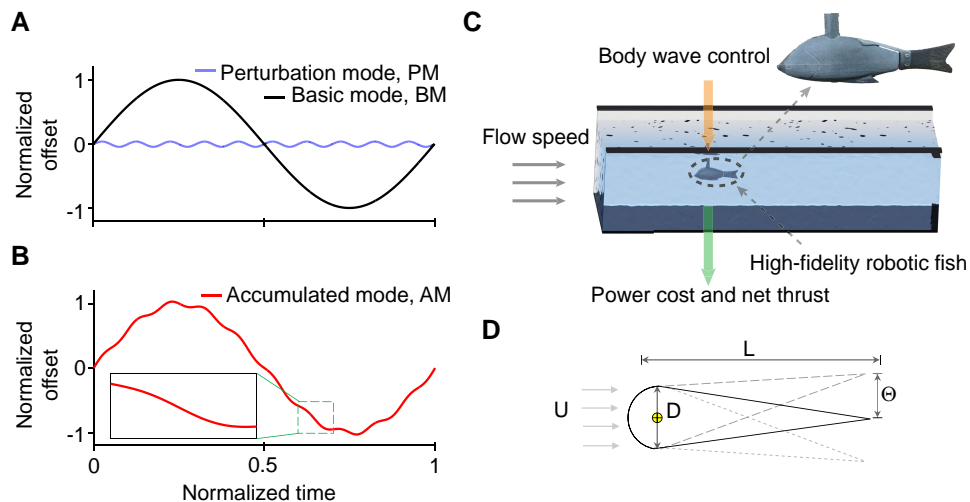
Fig. 1. A and B) Foil pitching angle variation in time for the periodic "basic mode" (BM), "perturbation mode" PM (controlled by $(\tilde{f}, \tilde{A}) = (10, 0.04)$), and "accumulated mode" AM (controlled by $(\tilde{f}, \tilde{A}) = (10, 0.04)$), respectively, where the time is normalized by $1/f_{bm}$. C) Sketch of the experiments in the flow tank with a high-fidelity robotic fish. The motion of the robotic fish's body wave was manipulated with and without perturbations (BM and AM), and the power cost and net thrust were measured. D) A tear-like foil is used to simplify the fish. The foil is of a length L and a head thickness D (diameter of the semicircle), where the pitching center is located at the center of the semicircle.

with a frequency of $f_{bm} = 1\,Hz$ and amplitude of $\Theta_{bm} = 0.349\,rad$, resulting in a Strouhal number of 0.32, similar to the Strouhal number employed by swimming fish (24–27). The corresponding Reynolds number $Re = UL/v$ is 1,900, where L is the body length and v is the kinematic viscosity of the fluid at a temperature of $20°$. In the experiments, we measured time-averaged net thrust $\bar{T}$, time-averaged power cost $\bar{P}$, and swimming (Froude) efficiency η ($= \bar{T}U/\bar{P}$) of the robotic fish in the BM and AM modes. The power cost, generated thrust, and efficiency ratios with perturbation to those without perturbation are defined as

$$\tilde{P} = (\bar{P}_{am} - \bar{P}_{bm})/\bar{P}_{bm} \quad \text{dimensionless power,}$$
$$\tilde{T} = (\bar{T}_{am} - \bar{T}_{bm})/\bar{T}_{bm} \quad \text{dimensionless thrust,} \quad (2)$$
$$\tilde{\eta} = (\eta_{am} - \eta_{bm})/\eta_{bm} \quad \text{dimensionless efficiency}$$

to quantitatively compare the performances under different modes.

Experiments were conducted with a perturbation of $(\tilde{f}, \tilde{A}) = (4, 0.3)$. We find $\tilde{P} = 265\%$, $\tilde{T} = 366\%$, and $\tilde{\eta} = 28\%$ (Fig. 2A–C; Movie S1), suggesting that introducing relatively high-frequency and low-amplitude perturbations to tailbeats can improve both net thrust and swimming efficiency simultaneously. To systematically explore how perturbation influences the fish propulsion, we further studied the function of perturbations with $\tilde{f}$ ranging from 4 to 6 and $\tilde{A}$ ranging from 0.1 to 0.3. As shown in Fig. 3A and B(i), both $\tilde{P}$ and $\tilde{T}$ are positively correlated with $\tilde{f}$ and/or $\tilde{A}$. This reveals that the stronger the perturbations, the higher the power costs, and the higher the generated net thrusts. Moreover, the normalized net thrust $\tilde{T}$ are all above 0, indicating that perturbations always improve net thrust. In contrast, Fig. 3C(i) indicates that the normalized efficiency $\tilde{\eta}$ has a complex relationship as a function of $\tilde{f}$ and $\tilde{A}$. In general, with fixed $\tilde{f}$ ($\tilde{A}$), an improvement of $\tilde{A}$ ($\tilde{f}$) will first improve and then inhibit $\tilde{\eta}$.
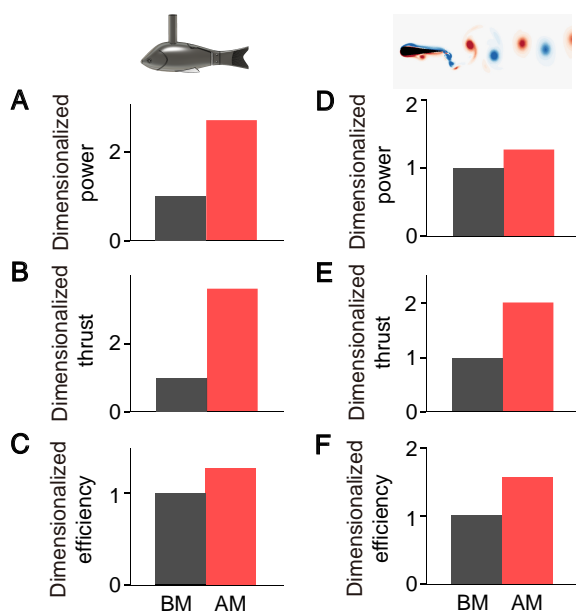
Fig. 2. A–C) Dimensionless time-averaged power, thrust, and efficiency of the robotic fish actuated in the BM and AM mode, respectively, where $(\tilde{f}, \tilde{A}, Re) = (4, 0.3, 1,900)$. D–F) Dimensionless time-averaged power, thrust, and efficiency of the numerical foil actuated in the BM and AM mode, respectively, where $(\tilde{f}, \tilde{A}, Re) = (10, 0.04, 1,000)$. For both experimental and numerical data, the quantities are normalized by the value produced by the BM mode.

Simulations on pitching foil

To explore the parameter space beyond the range of experimental capabilities, especially with respect to large variations in perturbations ($\tilde{f}$ and $\tilde{A}$) that would impose high torques on the actuators, we established a computational fluid dynamics simulation environment using FLUENT (ANSYS version 14.0). The simulations also enable a more comprehensive analysis of the flow profiles that result from superimposed perturbations and thus shed light on the hydrodynamic features underlying the observed trends. For simulations, we employed a simplified tear-like foil with the dimensionless thickness of $D/L = 0.196$ (D denotes foil thickness, Fig. 1D).

To validate the simulation model with respect to physical experiments, we conducted an investigation of the swimming performance of a pitching foil with a perturbation of $(\tilde{f}, \tilde{A}) = (10, 0.04)$ and a basic wave with frequency $f_{bm} = 2\,Hz$ and amplitude $\Theta_{bm} = 0.175\,rad$ at a Reynolds number of 10^3. In our simulations, we also observed that adding perturbations enhances both thrust and efficiency ($\tilde{P} = 27\%$, $\tilde{T} = 101\%$, and $\tilde{\eta} = 58\%$), consistent with our experimental findings (Fig. 2D–F; Movie S2).

To systematically explore the impact of perturbations over a wider range of parameters, we conducted simulations by varying $\tilde{f}$ ranging from 4 to 30, $\tilde{A}$ ranging from 0.04 to 0.4, for Reynolds numbers of 1,000, 2,500, and 5,000. Figure 3A–C(ii–iv) summarizes the results after over 80,000 core hours of simulations. We systematically explored the normalized power cost, net thrust, and swimming efficiency as a function of normalized frequency $\tilde{f}$ and amplitude $\tilde{A}$. With increasing in $\tilde{f}$ and/or $\tilde{A}$, $\tilde{P}$, and $\tilde{T}$ gradually increase, while $\tilde{\eta}$ first increases and then decreases. As expected, the numerical results conform to those obtained from the experiments, with deviations occurring due to features such as the difference in the profile of baseline tailbeat kinematics, differences in morphology, and differences in dimensions. The similarity in the trends of the improvement in efficiency noticed in both simulations and experiments suggests that the benefits of perturbations are robust and, therefore, could be generic. The optimal case of simulations is obtained at $(\tilde{f}, \tilde{A}, Re) = (4, 0.25, 10^3)$, resulting in $(\tilde{P}, \tilde{T}, \tilde{\eta}) = (196\%, 467\%, 92\%)$. Additionally, optimal lines for $\tilde{\eta}$ are formed as $\tilde{A} \sim \tilde{f}^{-1}$, indicating that significant improvement in $\tilde{\eta}$ could be achieved through high-frequency, low-amplitude perturbations and vice versa. Moreover, our numerical results also show that while all perturbations enhance thrust, not all perturbations improve efficiency. Using the power fitting method, we found that the lines formed as $\tilde{A} \sim \tilde{f}^{-1.5}$ (coefficient of determination $R^2 > 0.98$) distinguish between improvement and decline in efficiency.

Wake structures and moment analysis

To understand the interaction between pitching foil and flow induced by superimposed high-frequency and low-amplitude perturbations, we further studied the wake structures provided by both BM and AM to visualize the complex dynamics of fluids. At $tf_{bm} = 18$, we illustrated the contour of vorticity $\omega^* = \omega D/U$ using the numerical simulations results at $(\tilde{f}, \tilde{A}, Re) = (10, 0.04, 10^3)$, where ω is the spanwise vorticity. As shown in Fig. 4A, the basic mode (BM) generates 2S wakes (39), a typical reverse Bénard–von Kármán (rBvK) vortex street, leading to a jet-flow (Fig. S2A). In contrast, accumulated mode (AM) generated additional smaller eddies due to superimposing the perturbations (Fig. 4B), resulting in a deflected flow which slants upward first and then downward (Fig. S2B).

There are two stages during the vortex shedding: vortex development (VD) and vortex transportation (VT). VD, viewed as a precursor to VT, physically describes the process of vorticities feeding from the shear layer and is terminated when the generated vortex
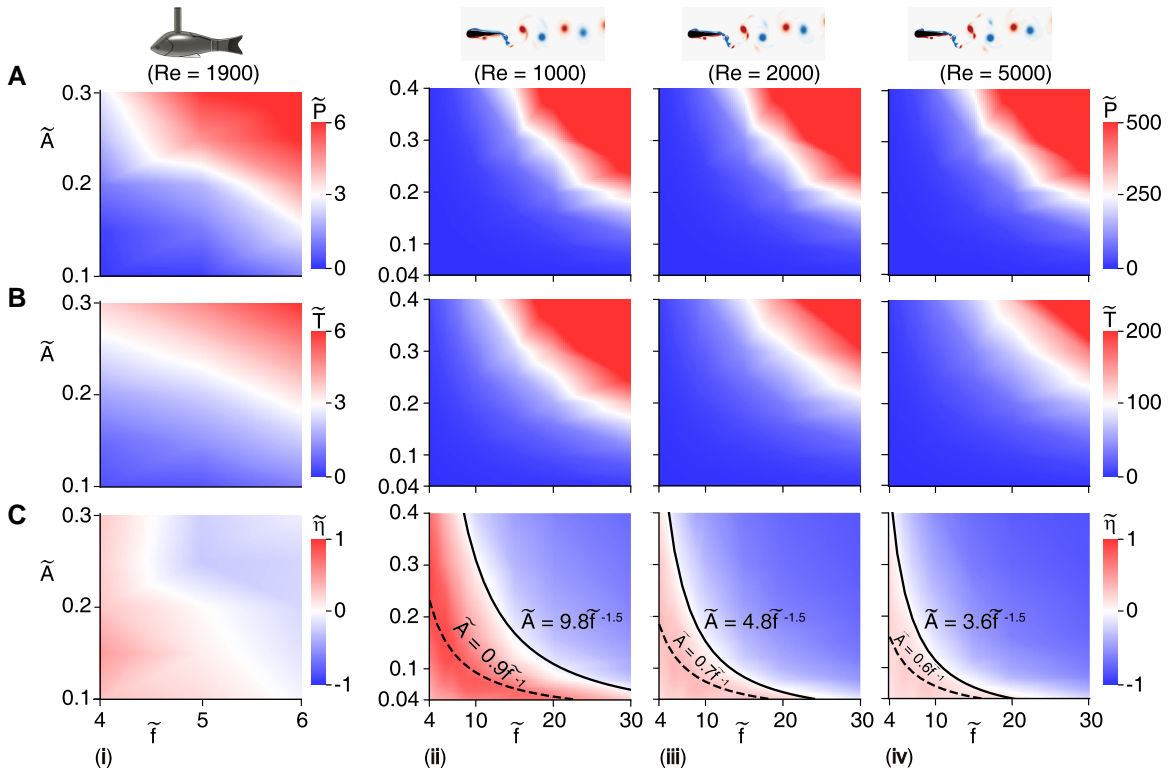
Fig. 3. Contours of A) $\tilde{P}$, B) $\tilde{T}$, and C) $\tilde{\eta}$ in the $\tilde{f}$–$\tilde{A}$ plane. (i) Experimental results at $Re = 1,900$. (ii–iv) Simulation results at $Re = 1,000, 2,500, 5,000$, respectively. In panel C(ii–iv), the dashed lines denote the fitting lines for the optimal $\tilde{\eta}$, where the coefficient of determination $R^2 = 0.962, 0.920$, and 0.882, correspond to $\tilde{A} = 0.9\tilde{f}^{-1.0}$, $\tilde{A} = 0.7\tilde{f}^{-1.0}$, and $\tilde{A} = 0.6\tilde{f}^{-1.0}$, respectively; the solid lines denote the fitting lines for $\tilde{\eta} = 0$, where $R^2 = 0.987, 0.997$, and 0.983 correspond to $\tilde{A} = 9.8\tilde{f}^{-1.5}$, $\tilde{A} = 4.8\tilde{f}^{-1.5}$, and $\tilde{A} = 3.6\tilde{f}^{-1.5}$, respectively. In simulations, $\eta_{bm} = 9.23, 15.04$, and 17.69% correspond to $Re = 1,000, 2,500$, and $5,000$, respectively.

can no longer entrain additional vorticity from the vortex generator (referred to as the vortex pinchoff) (40, 41). The vortex pinchoff occurs when the vortex possesses maximum energy from a vortex generator (42), or the vortex generator suddenly stops the energy injection into the vortex, such as the flapping oscillation considered in present work (43). The superimposed perturbations cause the foil to alter its flapping direction rapidly, and multiple vortex pinchoffs occur. As a result, the small-scale eddies provided by perturbations in the wake will be separated between the large-scale vortices generated by the basic oscillation, leading to variations in the positioning of dominant vortices (Fig. S3).

Since the time-averaged power cost can be calculated as $\bar{P} = f_{bm} \int_0^{1/f_{bm}} M_f(t)\dot{\theta}(t)dt$ (see Materials and methods for details), where $M_f(t)$ is the torque induced by fluid dynamics, it is worth understanding how $M_f(t)$ is affected by superimposed perturbations to demystify the mechanisms underlying efficiency improvements. Figure 5A reveals the $M_f(t)$ provided by BM remains the same frequency with $\ddot{\theta}(t)$, while the perturbation dominates $M_f(t)$ profile in AM. Particularly, a phase lag ϕ exists between $\ddot{\theta}(t)$ and $M_f(t)$. This ϕ described the phase lag between foil's oscillation and motion-induced fluid dynamics response is actually sourced from the "memory effect" in flow (44). Using the Hilbert transform, we calculated ϕ_{bm} and ϕ_{am} referred to BM-based and AM-based phase lag, respectively, and found $|\phi_{am}| < |\phi_{bm}|$. This discrepancy is attributed to the high-frequency components introduced by superimposed perturbations, which induce rapid transitions in pitching velocity, accelerate the diffusion–convection process in the vorticity layer created on the foil's surface after a change in velocity, and thus facilitate an efficient response of the fluid dynamics to the pitching oscillation.
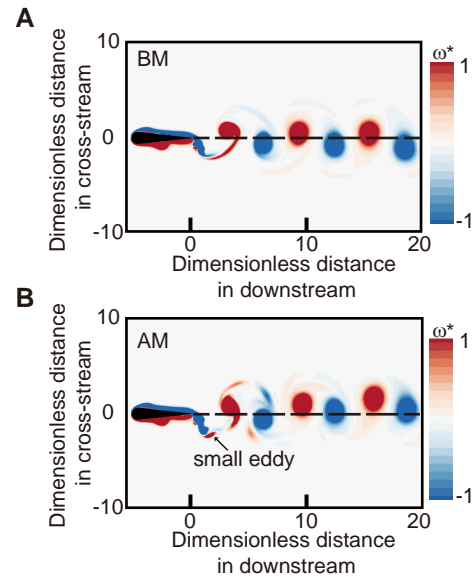
Fig. 4. Flow patterns of the foil in A) BM and B) AM, where the red and blue colors denote positive and negative vorticities, respectively. $\omega^* = \omega D/U$, where ω is the spanwise vorticity ($\tilde{f}, \tilde{A}, Re) = (10, 0.04, 1,000)$.

Mathematically, the minimal $\bar{P}$ will be achieved when $M_f(t)$ and $\dot{\theta}(t)$ are out-of-phase, which corresponds to $M_f(t)$ and $\ddot{\theta}(t)$ being in-phase, i.e. $\phi = 0$. On the other hand, a smaller phase lag between fluid and flow-driven motion is thought to be beneficial for enhancing the energy harvesting efficiency in a flow-induced vibration

A

B
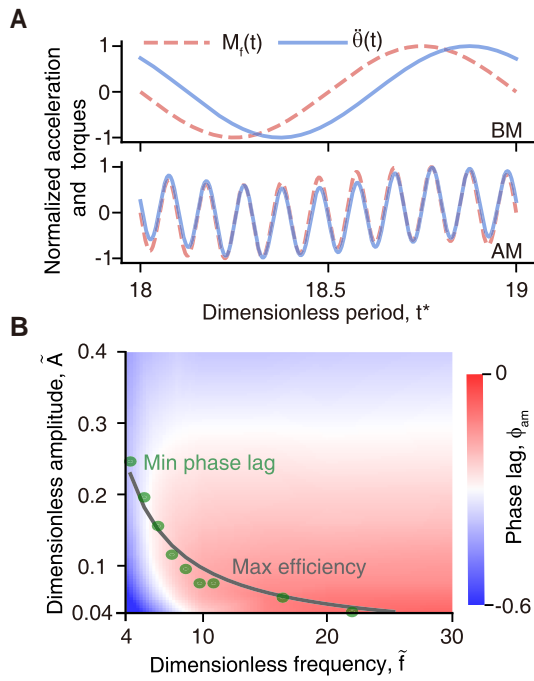
Fig. 5. A) Normalized foil pitching acceleration $\ddot{\theta}(t)$ and flow-induced torque $M_f(t)$ in BM and AM, respectively, where $(\tilde{f}, \tilde{A}, Re) = (10, 0.04, 1,000)$. B) The ϕ_{am} contour in $\tilde{f} - \tilde{A}$ plane at $Re = 1,000$, where the solid line refers to the optimal efficiency improvement line in Fig. 3C(ii) and the circle symbol denotes the location of the minimal $|\phi_{am}|$ at the specific $\tilde{f}$.

system (45). Figure 5B implies that ϕ_{am} is a function of $\tilde{f}$ and $\tilde{A}$ and the minimal $|\phi_{am}|$ values agree well with the data-driven optimal $\tilde{\eta}$ line in Fig. 3C(ii). This result reveals that phase lag is a critical parameter in affecting efficiency production, a smaller ϕ would cause less energy consumption and potentially improve swimming efficiency.

Analytical models

To explore the mechanisms underlying the improvements in propulsive thrust and swimming efficiency, we further presented analytical models to examine the correlation between dimensionless thrust and efficiency, and the dimensionless frequency and amplitude.

The time-averaged thrust acting on the foil $\bar{T}$ is the sum of the time-averaged pressure-induced thrust $\bar{T}^P (> 0)$ and time-averaged viscous drag $\bar{T}^V (< 0)$, as

$$\bar{T} = \bar{T}^P + \bar{T}^V. \tag{3}$$

Inspired by previous works on pitching foils (31, 46, 47), the time-averaged pressure-induced thrusts read as

$$\begin{aligned} \bar{T}^P_{bm} &\sim \rho U^2 S_f St_{bm}^2 \quad \text{in BM,} \\ \bar{T}^P_{am} &\sim \rho U^2 S_f (St_{bm}^2 + St_{pm}^2) \quad \text{in AM,} \end{aligned} \tag{4}$$

where S_f denotes the surface area of the foil, while

$$\begin{aligned} \bar{T}^V_{bm} &\sim -\rho U^2 S_f Re^{-\frac{1}{2}} \sqrt{St_{bm}} \quad \text{in BM,} \\ \bar{T}^V_{am} &\sim -\rho U^2 S_f Re^{-\frac{1}{2}} \sqrt{St_{bm} + St_{pm}} \quad \text{in AM} \end{aligned} \tag{5}$$

can be driven from the Bone–Lighthill boundary-layer thinning hypothesis (48, 49). Equation 5 reveals the magnitude of viscous drag produced by the AM is slightly larger than that produced by the BM ($\bar{T}^V_{am}/\bar{T}^V_{bm} \sim \sqrt{1 + \tilde{St}}$). At $(\tilde{f}, \tilde{A}, Re) = (10, 0.04, 10^3)$, we found $\bar{T}^V_{am}/\bar{T}^V_{bm} > 1$ (Fig. S4), agreeing with the theoretical

prediction. The increase of viscous drag undergoing the AM is owed to the compression of the shear layer and the acceleration of the tangential component of the potential outer flow near the foil. With increasing in Re, $\bar{T}^V$ approaches zero (Eq. 5), suggesting the pressure-induced thrust dominates the thrust generation (50, 51). We thus have

$$\tilde{T} \sim \tilde{St}^2 \tag{6}$$

when the viscous effect is neglected ($Re \to \infty$). As the perturbations introduce the dimensionless amplitude and frequency, the Strouhal number ratio $\tilde{St}$ also increases ($\tilde{St} > 0$), and thus time-averaged thrust is improved ($\tilde{T} > 0$, Fig. 3B). Equation 6 further reveals the thrust enhancement in AM is mainly sourced from the increase of pressure-induced thrust (Fig. S4).

We next derive the dimensionless efficiency as a function of the dimensionless frequency and amplitude. To do so, we also need to estimate dimensionless power cost, as

$$\begin{aligned} \bar{P} &= f_{bm} \int_0^{1/f_{bm}} [M_i(t) - M_f(t)] \times \dot{\theta}(t) \, dt \\ &= f_{bm} \int_0^{1/f_{bm}} M_f(t) \dot{\theta}(t) \, dt, \end{aligned} \tag{7}$$

where $M_i(t) = J\ddot{\theta}(t)$ is the inertia torque with the mass moment of inertia of the foil J, the $M_f(t)$ is calculated as $M_f(t) = -c_1\ddot{\epsilon}(t) - c_2 U\dot{\epsilon}(t)$ with two positive coefficients $c_1 \sim L^4$ and $c_2 \sim L^3$ (L represents body length), $\dot{\epsilon}(t) = \dot{\theta}(t + \phi)$ and $\ddot{\epsilon}(t) = \ddot{\theta}(t + \phi)$ refer to the angular velocity and acceleration of the fluid around the foil, respectively (46). Then, we have the $\tilde{P}$ scaling as (see Materials and methods for details)

$$\tilde{P} \sim \frac{(\tilde{A}^{-1}\tilde{St}^3 + 1)\sin(\phi_{am})}{\sin(\phi_{bm})} - 1 \tag{8}$$

when $A_{pm} \approx 0$ is caused by the low-amplitude pitching.

As a result, we obtain the efficiency $\tilde{\eta}$ scaling as (see Materials and methods for details)

$$\tilde{\eta} \sim \frac{(\tilde{St}^2 + 1)\sin(\phi_{bm})}{(\tilde{A}^{-1}\tilde{St}^3 + 1)\sin(\phi_{am})} - 1 \tag{9}$$

when $Re \to \infty$ and $A_{pm} \to 0$. Equation 9 reveals a smaller ϕ_{am} would lead to a larger $\tilde{\eta}$ with a special $\tilde{St}$ and $\tilde{A}$.

The analytical models are verified by comparing to both experimental and simulation results in Fig. 6. The scaling equations degenerate as $\tilde{T} = 0$, $\tilde{P} = 0$ and $\tilde{\eta} = 0$, respectively, when no perturbations have been added ($\tilde{St} = 0$, and $\phi_{bm} = \phi_{am}$).

Discussion and conclusion

Swimming is energetically expensive and animals and robots need efficient kinematic strategies to increase the thrust produced and maximize their locomotion efficiency. This study investigates the impact of introducing kinematic perturbations to the rhythmic tailbeat of fish-like swimming oscillators. By systematically varying the profile of the perturbation in relation to the kinematics, we find that superimposing perturbations consistently increase thrust but not swimming efficiency. Given that only particular perturbations enhance both thrust and efficiency, our study suggests that previous conflicting results may arise from variations in parameter spaces (37, 38).

The mechanism we found for improving efficiency complements previous studies. Prior research has suggested that the optimal swimming efficiency is determined by the fluid drag on fins
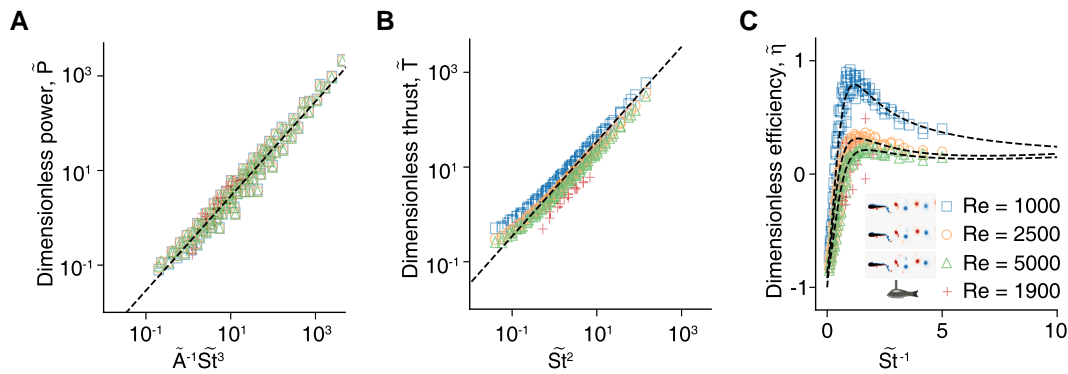
Fig. 6. Scaling for the dimensionless A) power $\tilde{P}$, B) thrust $\tilde{T}$, and C) efficiency $\tilde{\eta}$. Dashed lines refer to the scaling lines derived from Eqs. 8, 6, and 9, respectively.

and wings, with a lower drag resulting in a higher efficiency (52). However, in our case, we found that superimposing perturbations leads to higher viscous drag but still improves efficiency (Eq. 5; Fig. S4). Another previously proposed way to enhance swimming efficiency is to increase the maximal angle of attack (AoA) below the dynamic stall limit, which prevents the shedding of leading-edge vortices (52, 53). In our study, perturbations, particularly those with small amplitudes, do not noticeably enhance the maximal AoA (Eq. 1); therefore, the efficiency gain from perturbations is not attributable to increased maximal AoA. Additionally, the efficiency improvement may be due to resonance between the natural frequency of the oscillating system and the frequency of vortex shedding (54). We cannot reject the hypothesis corresponding to the resonance effects since reducing the phase lag between body motion and fluid dynamics responses also affects the frequency of vortex shedding.

According to Granger and Paidoussis (44), the phase lag is likely caused by the flow retardation effect, which results in a reorganization of the flow around the body, leading to a time delay between body motion and fluid dynamics response, known as the phase lag. This is different from the time delay caused by the Wagner effect (55) (also known as the "start vortex effect") as the phase lag maintains after the initialization. As the Reynolds number increases, the boundary layer becomes thinner, which in turn diminishes the rate of acceleration for the diffusion–convection of the vorticity. This leads to a smaller reduction of phase lag and thus lower efficiency improvement. Therefore, the higher the Reynolds number, the smaller the improvement in efficiency. Our findings in Fig. 6C are consistent with this, as we observe that the efficiency improvement from certain superimposed perturbations becomes insignificant at higher Reynolds numbers. On the other hand, as *Re* increases, it would result in a reduction in efficiency improvement since the swimming efficiency provided by the BM increases with increasing in *Re* (50). This further indicates that superimposed perturbations to improve locomotion may be more beneficial for larval fish than adult fish, since the viscosity has a greater impact on larvae (56). These findings could also explain why larval fish exhibit more random body waves while adults exhibit clearer stereotypical sinusoidal tailbeat kinematics (57).

Further examination of the impact of more general perturbations on thrust and efficiency will be beneficial. Specifically, investigating the effects of nonkinematic higher frequency and lower amplitude random perturbations, which more accurately replicate the perturbations that animals experience in the wild, such as those caused by turbulence during flight or swimming, will be useful. The findings and analytical models presented here lay the foundation for extending to practical applications that can

effectively introduce kinematic perturbation to deliver thrust and efficiency improvements to general underwater robots or gliders.

Materials and methods
Experimental setup and procedure
Figure 1C shows a schematic of the experimental setup. The experiments were conducted at the Max Planck Institute of Animal Behavior using a flow tank with dimensions of $250 \times 875 \times 250$ millimeters (mm) in width, length, and depth. The flow speed was calibrated to be linearly proportional to the control voltage. Our robotic fish models were designed according to the morphology of the goldfish with a body length of 15 cm. We first scanned real fish to obtain the 3D fish body as a point cloud map. Reverse modeling of the mesh from the cloud map was utilized for our mechanical design using SolidWorks, and the fish body was printed with a 3D printer (Ultimaker S3). Limited by the size of the real fish, we included a single joint in this robot design. The oscillation of this joint is controlled by a waterproof servomotor (Hitec HS-5086WP) driven by a central pattern generator control (58).

Thrust $T(t)$ was measured using a force balance with a full-scale range of 5 kg (Z6FD1, Deutschland HBM). Power $P(t)$ was calculated as the input energy of the motion-generated motor. Data were sampled at a rate of 5,000 points per second using a current acquisition system (NI-9227, National Instruments). Each experimental trial consisted of a 5-s initialization period, during which the robotic fish swam to establish the vortex stream, followed by a 5-s data collection period. To ensure reliability, each set of parameters was repeated five times. For the base mode, we find $P_{\text{bm}} = 0.775$ W, $T_{\text{bm}} = 0.183$ N, $\eta_{\text{bm}} = T_{\text{bm}}/P_{\text{bm}} = 0.236$ N/W.

Simulations
In our study, we adopted the mesh system and numerical method previously used by Muhammad et al. (35). The computational domain used in the simulations is shown in Fig. S6. The foil's geometry was defined using the same parameters as in Fig. 1D. The computational domain is a 2D rectangular region with dimensions of $200D \times 100D$, where D is the foil thickness. The inlet velocity boundary condition is located at a distance of $50D$ from the pitching center of the foil, with a velocity vector $(U, 0)$. The outflow boundary is situated $150D$ downstream, with no-stress outflow boundary conditions. The upper and lower boundaries are slip walls located $50D$ apart from the foil. The computational domain is divided into three grid zones: Zone 1, Zone 2, and Zone 3. Zone 1, inside the blue circle region, has a high grid resolution around the

foil. Zone 1 is given an O-xy mesh system where the grids move with the foil as a rigid body. In Zone 1, the first cell is placed at a distance of $0.004D$ from the foil surface. Zone 2, the black region, has a high resolution to capture large velocity gradients. The blue circle is a circular nonconformal sliding grid interface. It is the interface between Zone 1 and Zone 2. Zone 3, located away from the wake region, has a medium resolution. Zones 2 and 3 employ structured meshes. The prescribed motion of Eq. 1 is controlled using a user defined function with the DEFINE _CG _MOTION function.

The grid and time-step independence tests were performed to validate the numerical simulations at the most strenuous parameters $(\tilde{f}, \tilde{A}) = (30, 0.40)$ with Reynolds number of $Re = 5 \times 10^3$. Figure S7 shows the results. The grid independence test is done for three sets of grids with 1.14×10^5 (G1), 2.13×10^5 (G2), and 4.18×10^5 (G3) corresponding to 233, 350, and 525 points on the foil surface, respectively. The time-step of $\Delta t = 1/(2,000 f_{pm})$ in the grid independence test is decided by Muhammad et al. (35) and the empirical formula ($\Delta t = \min\{1/(2,000 f_{pm}), L/\|V\|\}$, where $\|V\|$ is the maximal instantaneous convective flux velocity in the computational domain) proposed by Kinsey and Dumas (59). The dimensionless instantaneous thrust (by $\bar{T}_{bm}$) over one pitching period ($1/f_{bm}$) for the three grid systems show no obvious difference is observed between G2 and G3 (Fig. S7A and Table S1). The difference in the dimensionless time-averaged thrust (by $\bar{T}_{bm}$) between G2 and G3 is reasonably small, as 0.65%. Mesh G2 is thus adopted. With G2, three time-steps $\Delta t_1 = 1/(1,000 f_{pm})$, $\Delta t_2 = 1/(2,000 f_{pm})$, and $\Delta t_3 = 1/(4,000 f_{pm})$ are tested. The result of dimensionalized instantaneous thrust reveals the difference in the dimensionless time-averaged thrust between Δt_2 and Δt_3 is only 0.53% (Fig. S7B and Table S2). Considering the accuracy and computational resources, Δt_2 is chosen for the extensive work.

In our simulation, the simulation is performed using a grid number of 2.13×10^5, corresponding to 350 points on the foil surface, and a time-step $\Delta t = 1/(2,000 f_{pm})$. To ensure statistically steady thrust and wake structures, all simulations are run for 20 pitching periods ($1/f_{bm}$), and the averages are calculated over the final 5 simulation periods after achieving statistical convergence. For the base mode, we find ($P_{bm}/0.5\rho U^3 L$, $T_{bm}/0.5\rho U^2 L$, η_{bm} = 0.068, 0.006, 0.092) at $Re = 1,000$, ($P_{bm}/0.5\rho U^3 L$, $T_{bm}/0.5\rho U^2 L$, η_{bm} = 0.071, 0.011, 0.15) at $Re = 2500$, and ($P_{bm}/0.5\rho U^3 L$, $T_{bm}/0.5\rho U^2 L$, η_{bm} = 0.072, 0.013, 0.177) at $Re = 5,000$, where $\eta_{bm} = T_{bm}U/P_{bm}$, respectively.

Models

In Eq. 3, $\bar{T}^P$ reads as

$$\bar{T}^P \sim f_{bm} \int_0^{1/f_{bm}} \rho S_f \times \dot{\epsilon}^2(t) \times \cos[\theta(t)] \, dt. \tag{10}$$

Here, S_f denotes the surface area of the foil, $\dot{\epsilon}(t)$ is the angular velocity of the fluid around the foil. As introduced before, a phase lag ϕ exits between $\theta(t)$ and $\epsilon(t)$, we thus have

$$\begin{aligned} \dot{\epsilon}_{bm}(t) &= 2\pi f_{bm}\Theta_{bm}\cos(2\pi f_{bm}t + \phi_{bm}), \\ \dot{\epsilon}_{am}(t) &= 2\pi[f_{bm}\Theta_{bm}\cos(2\pi f_{bm}t + \phi_{am}) \\ &\quad + f_{pm}\Theta_{pm}\cos(2\pi f_{pm}t + \phi_{am})] \end{aligned} \tag{11}$$

corresponding to BM and AM, respectively. Considering a small Θ_{bm} and even smaller Θ_{pm}, we get $\cos[\theta_{bm}(t)] \approx \cos[\theta_{am}(t)] \approx 1$ (Fig. S8), and $\Theta_{pm}/\Theta_{am} \approx A_{pm}/A_{bm} = \tilde{A}$. Therefore, the time-averaged pressure thrusts read as Eq. 4.

The time-averaged viscous drag can be estimated using results of the works on the Bone–Lighthill boundary-layer thinning hypothesis (48, 49), as Eq. 5.

We thus have

$$\tilde{T} \sim \frac{\tilde{S}t^2 - \frac{1}{c_0}St_{bm}^{-\frac{3}{2}}Re^{-\frac{1}{2}}(\sqrt{\tilde{S}t + 1} - 1)}{1 - \frac{1}{c_0}St_{bm}^{-\frac{3}{2}}Re^{-\frac{1}{2}}} \tag{12}$$

with a positive constant c_0. Particularly, when the viscous effect is neglected ($Re \to \infty$), Eq. 12 degenerates as Eq. 6.

We next derive the dimensionless efficiency as a function of the dimensionless frequency and amplitude. The time-averaged power cost is considered as the product of the net torque $M(t) = M_i(t) - M_f(t)$ and $\ddot{\theta}(t)$ on the pitching foil, i.e. as introduced before, we get Eq. 7.

For BM and AM, the net torque $M(t)$ can be calculated as

$$\begin{aligned} M_{bm}(t) = &-(4\pi^2)Jf_{bm}^2\Theta_{bm}\sin(2\pi f_{bm}t) \\ &-(4\pi^2)c_1 f_{bm}^2\Theta_{bm}\sin(2\pi f_{bm}t + \phi_{bm}) \\ &+(2\pi)c_2 U f_{bm}\Theta_{bm}\cos(2\pi f_{bm}t + \phi_{bm}), \end{aligned} \tag{13}$$

and

$$\begin{aligned} M_{am}(t) = &-(4\pi^2)J[f_{bm}^2\Theta_{bm}\sin(2\pi f_{bm}t) \\ &+ f_{pm}^2\Theta_{pm}\sin(2\pi f_{pm}t)] \\ &-(4\pi^2)c_1[f_{bm}^2\Theta_{bm}\sin(2\pi f_{bm}t + \phi_{am}) \\ &+ f_{pm}^2\Theta_{pm}\sin(2\pi f_{pm}t + \phi_{am})] \\ &+(2\pi)c_2 U[f_{bm}\Theta_{bm}\cos(2\pi f_{bm}t + \phi_{am}) \\ &+ f_{pm}\Theta_{pm}\cos(2\pi f_{pm}t + \phi_{am})], \end{aligned} \tag{14}$$

respectively. The $\dot{\theta}(t)$ can be directly obtained from the kinematics (Eq. 1), as

$$\begin{aligned} \dot{\theta}_{bm}(t) &= 2\pi f_{bm}\Theta_{bm}\cos(2\pi f_{bm}t) \quad \text{in BM,} \\ \dot{\theta}_{am}(t) &= 2\pi[f_{bm}\Theta_{bm}\cos(2\pi f_{bm}t) \\ &\quad + f_{pm}\Theta_{pm}\cos(2\pi f_{pm}t)] \quad \text{in AM.} \end{aligned} \tag{15}$$

Since $\int_0^{1/f_{bm}} M_i(t)\dot{\theta}(t)dt = \int_0^{1/f_{bm}} J\ddot{\theta}(t)\dot{\theta}(t)dt = 0$. The power cost is actually the integral of the product of $M_f(t)$ and $\dot{\theta}(t)$. Through substituting Eqs. 13–15 into Eq. 7, the time-averaged power cost reads as

$$\begin{aligned} \bar{P}_{bm}(t) \sim &-c_3 L f_{bm}^3\Theta_{bm}^2\sin(\phi_{bm}) \\ &+ U f_{bm}^2\Theta_{bm}^2\cos(\phi_{bm}) \quad \text{in BM,} \\ \bar{P}_{am}(t) \sim &-c_3 L(f_{bm}^3\Theta_{bm}^2 + f_{pm}^3\Theta_{pm}^2)\sin(\phi_{am}) \\ &+ U(f_{bm}^2\Theta_{bm}^2 + f_{pm}^2\Theta_{pm}^2)\cos(\phi_{am}) \quad \text{in AM} \end{aligned} \tag{16}$$

with the positive coefficient c_3. Then, we have the $\tilde{P}$ scaling as

$$\tilde{P} \sim \frac{-c_3 L St_{bm}(\tilde{A} + \tilde{S}t^3)\sin(\phi_{am}) + A_{pm}(1 + \tilde{S}t^2)\cos(\phi_{am})}{-c_3 L\tilde{A}St_{bm}\sin(\phi_{bm}) + A_{pm}\cos(\phi_{bm})} - 1. \tag{17}$$

Note $A_{pm} \approx 0$ caused by the low-amplitude pitching, the Eq. 17 can therefore be simplified as Eq. 8.

As a result, we obtain the efficiency $\tilde{\eta}$ scaling as

$$\begin{aligned} \tilde{\eta} = \frac{\tilde{T} + 1}{\tilde{P} + 1} - 1 \sim &\frac{(\tilde{S}t^2 + 1) - \frac{1}{c_0}St_{bm}^{-\frac{3}{2}}Re^{-\frac{1}{2}}(\sqrt{\tilde{S}t + 1})}{1 - \frac{1}{c_0}St_{bm}^{-\frac{3}{2}}Re^{-\frac{1}{2}}} \\ &\times \frac{-c_3 L\tilde{A}\sin(\phi_{bm}) + A_{pm}St_{bm}^{-1}\cos(\phi_{bm})}{-c_3 L(\tilde{S}t^3 + \tilde{A})\sin(\phi_{am}) + A_{pm}St_{bm}^{-1}(\tilde{S}t^2 + 1)\cos(\phi_{am})} - 1. \end{aligned} \tag{18}$$

In particular, when $Re \to \infty$ and $A_{pm} \to 0$, we get Eq. 9.

Supplementary Material

Supplementary material is available at *PNAS Nexus* online.

Funding

Author Contributions

L.-M.C. and L.L. conceived the idea and designed the project. L.-M.C. carried out the simulations. L.-M.C., S.W., and L.L. performed the experiments. L.-M.C. and L.J. formulated the mathematical model. L.-M.C., L.J., S.W., A.L., S.R., I.D.C., and L.L. analyzed the data. All authors contributed to writing the paper.

Previous Presentation

These results have not been presented previously.

Data Availability

The data that support the findings of this study are available in figshare with the identifier https://doi.org/10.6084/m9.figshare.25272523. Source data are provided with this paper.

References

1 Lighthill MJ. 1969. Hydromechanics of aquatic animal propulsion. *Annu Rev Fluid Mech*. 1(1):413–446.

2 Ristroph L, Liao JC, Zhang J. 2015. Lateral line layout correlates with the differential hydrodynamic pressure on swimming fish. *Phys Rev Lett*. 114(1):018102.

3 Triantafyllou MS, Triantafyllou GS, Yue DKP. 2000. Hydrodynamics of fishlike swimming. *Annu Rev Fluid Mech*. 32(1):33–53.

4 Fish FE, Lauder GV. 2006. Passive and active flow control by swimming fishes and mammals. *Annu Rev Fluid Mech*. 38:193–224.

5 Wu TY. 2011. Fish swimming and bird/insect flight. *Annu Rev Fluid Mech*. 43:25–58.

6 Oeffner J, Lauder GV. 2012. The hydrodynamic function of shark skin and two biomimetic applications. *J Exp Biol*. 215(5):785–795.

7 Wen L, Weaver JC, Lauder GV. 2014. Biomimetic shark skin: design, fabrication and hydrodynamic function. *J Exp Biol*. 217(10): 1656–1666.

8 Lauder GV, *et al.* 2016. Structure, biomimetics, and fluid dynamics of fish skin surfaces. *Phys Rev Fluids*. 1(6):060502.

9 Weihs D. 1973. Hydromechanics of fish schooling. *Nature*. 241(5387):290–291.

10 Zhu X, He G, Zhang X. 2014. Flow-mediated interactions between two self-propelled flapping filaments in tandem configuration. *Phys Rev Lett*. 113(23):238105.

11 Becker AD, Masoud H, Newbolt JW, Shelley M, Ristroph L. 2015. Hydrodynamic schooling of flapping swimmers. *Nat Commun*. 6(1):8514.

12 Filella A, Nadal F, Sire C, Kanso E, Eloy C. 2018. Model of collective fish behavior with hydrodynamic interactions. *Phys Rev Lett*. 120(19):198101.

13 Oza AU, Ristroph L, Shelley MJ. 2019. Lattices of hydrodynamically interacting flapping swimmers. *Phys Rev X*. 9(4):041024.

14 Li L, *et al.* 2020. Vortex phase matching as a strategy for schooling in robots and in fish. *Nat Commun*. 11(1):5408.

15 Prempraneerach P, Hover FS, Triantafyllou MS. 2003. The effect of chordwise flexibility on the thrust and efficiency of a flapping foil. In: Proceedings of the 13th International Symposium on Unmanned Untethered Submersible Technology: Special Session on Bioengineering Research Related to Autonomous Underwater Vehicles; New Hampshire. Vol. 152. Lee (NH): The Autonomous Undersea Systems Institute. p. 152–170.

16 Quinn DB, Lauder GV, Smits AJ. 2014. Scaling the propulsive performance of heaving flexible panels. *J Fluid Mech*. 738:250–267.

17 Quinn DB, Lauder GV, Smits AJ. 2015. Maximizing the efficiency of a flexible propulsor using experimental optimization. *J Fluid Mech*. 767:430–448.

18 Zhong Q, *et al.* 2021. Tunable stiffness enables fast and efficient swimming in fish-like robots. *Sci Robot*. 6(57):eabe4088.

19 Kern S, Koumoutsakos P. 2006. Simulations of optimized anguilliform swimming. *J Exp Biol*. 209(24):4841–4857.

20 Izraelevitz JS, Triantafyllou MS. 2014. Adding in-line motion and model-based optimization offers exceptional force control authority in flapping foils. *J Fluid Mech*. 742:5–34.

21 Maertens AP, Gao A, Triantafyllou MS. 2017. Optimal undulatory swimming for a single fish-like body and for a pair of interacting swimmers. *J Fluid Mech*. 813:301–345.

22 Chao L-M, Alam MM, Cheng L. 2022. Hydrodynamic performance of slender swimmer: effect of travelling wavelength. *J Fluid Mech*. 947:A8.

23 Smits AJ. 2019. Undulatory and oscillatory swimming. *J Fluid Mech*. 874:P1.

24 Taylor GK, Nudds RL, Thomas ALR. 2003. Flying and swimming animals cruise at a Strouhal number tuned for high power efficiency. *Nature*. 425(6959):707–711.

25 Rohr JJ, Fish FE. 2004. Strouhal numbers and optimization of swimming by odontocete cetaceans. *J Exp Biol*. 207(10):1633–1642.

26 Eloy C. 2012. Optimal Strouhal number for swimming animals. *J Fluids Struct*. 30:205–218.

27 Gazzola M, Argentina M, Mahadevan L. 2014. Scaling macroscopic aquatic locomotion. *Nat Phys*. 10(10):758–761.

28 Triantafyllou MS, Triantafyllou GS, Gopalkrishnan R. 1991. Wake mechanics for thrust generation in oscillating foils. *Phys Fluids A Fluid Dyn*. 3(12):2835–2837.

29 Anderson JM, Streitlien K, Barrett DS, Triantafyllou MS. 1998. Oscillating foils of high propulsive efficiency. *J Fluid Mech*. 360: 41–72.

30 Saadat M, *et al.* 2017. On the rules for aquatic locomotion. *Phys Rev Fluids*. 2(8):083102.

31 Floryan D, Van Buren T, Rowley CW, Smits AJ. 2017. Scaling the propulsive performance of heaving and pitching foils. *J Fluid Mech*. 822:386–397.

32 Lu K, Xie YH, Zhang D. 2013. Numerical study of large amplitude, nonsinusoidal motion and camber effects on pitching airfoil propulsion. *J Fluids Struct*. 36:184–194.

33 Van Buren T, Floryan D, Quinn D, Smits AJ. 2017. Nonsinusoidal gaits for unsteady propulsion. *Phys Rev Fluids*. 2(5):053101.

34 Chao L-M, Alam MM, Ji C. 2021. Drag–thrust transition and wake structures of a pitching foil undergoing asymmetric oscillation. *J Fluids Struct*. 103:103289.

35 Muhammad Z, Alam MM, Noack BR. 2022. Efficient thrust enhancement by modified pitching motion. *J Fluid Mech*. 933:A13.

36 Videler JJ, Hess F. 1984. Fast continuous swimming of two pelagic predators, saithe (*Pollachius virens*) and mackerel (*Scomber scombrus*): a kinematic analysis. *J Exp Biol*. 109(1):209–228.

37 Lehn AM, Thornycroft PJM, Lauder GV, Leftwich MC. 2017. Effect of input perturbation on the performance and wake dynamics of aquatic propulsion in heaving flexible foils. *Phys Rev Fluids*. 2(2): 023101.

38 Gao P, Huang Q, Pan G. 2021. Propulsion performance and wake dynamics of heaving foils under different waveform input perturbations. *J Mar Sci Eng*. 9(11):1271.

39 Williamson CHK, Roshko A. 1988. Vortex formation in the wake of an oscillating cylinder. *J Fluids Struct*. 2(4):355–381.

40 Dabiri JO. 2009. Optimal vortex formation as a unifying principle in biological propulsion. *Annu Rev Fluid Mech*. 41:17–33.

41 Yang A-l, Jia L-b, Yin X-z. 2012. Formation process of the vortex ring generated by an impulsively started circular disc. *J Fluid Mech*. 713:61–85.

42 Gharib M, Rambod E, Shariff K. 1998. A universal time scale for vortex ring formation. *J Fluid Mech*. 360:121–140.

43 Rival D, Prangemeier T, Tropea C. 2009. The influence of airfoil kinematics on the formation of leading-edge vortices in bio-inspired flight. *Exp Fluids*. 5(46):823–833.

44 Granger S, Paidoussis MP. 1996. An improvement to the quasi-steady model with application to cross-flow-induced vibration of tube arrays. *J Fluid Mech*. 320:163–184.

45 Han P, Huang W-X, Qin D, Wang J, Zhao J. 2023. An analytical model for estimating the maximum energy harvesting efficiency from vortex-induced vibration. *J Fluids Struct*. 122:103961.

46 Alam MM, Muhammad Z. 2020. Dynamics of flow around a pitching hydrofoil. *J Fluids Struct*. 99:103151.

47 Mackowski AW, Williamson CHK. 2015. Direct measurement of thrust and efficiency of an airfoil undergoing pure pitching. *J Fluid Mech*. 765:524–543.

48 Ehrenstein U, Eloy C. 2013. Skin friction on a moving wall and its implications for swimming animals. *J Fluid Mech*. 718:321–346.

49 Ehrenstein U, Marquillie M, Eloy C. 2014. Skin friction on a flapping plate in uniform flow. *Philos Trans R Soc A: Math Phys Eng Sci*. 372(2020):20130345.

50 Das A, Shukla RK, Govardhan RN. 2016. Existence of a sharp transition in the peak propulsive efficiency of a low-pitching foil. *J Fluid Mech*. 800:307–326.

51 Senturk U, Smits AJ. 2019. Reynolds number scaling of the propulsive performance of a pitching airfoil. *AIAA J*. 57(7): 2663–2669.

52 Floryan D, Van Buren T, Smits AJ. 2018. Efficient cruising for swimming and flying animals is dictated by fluid drag. *Proc Natl Acad Sci U S A*. 115(32):8116–8118.

53 Wang ZJ. 2000. Vortex shedding and frequency selection in flapping flight. *J Fluid Mech*. 410:323–341.

54 Moored KW, Dewey PA, Smits AJ, Haj-Hariri H. 2012. Hydrodynamic wake resonance as an underlying principle of efficient unsteady propulsion. *J Fluid Mech*. 708:329–348.

55 Sane SP. 2003. The aerodynamics of insect flight. *J Exp Biol*. 206(23):4191–4208.

56 Muller UK, Stamhuis EJ, Videler JJ. 2000. Hydrodynamics of unsteady fish swimming and the effects of body size: comparing the flow fields of fish larvae and adults. *J Exp Biol*. 203(2):193–206.

57 Muller UK, van Leeuwen JL. 2004. Swimming of larval zebrafish: ontogeny of body waves and implications for locomotory development. *J Exp Biol*. 207(5):853–868.

58 Li L, Wang C, Xie G. 2015. A general CPG network and its implementation on the microcontroller. *Neurocomputing*. 167:299–305.

59 Kinsey T, Dumas G. 2008. Parametric study of an oscillating airfoil in a power-extraction regime. *AIAA J*. 46(6):1318–1330.